

Simulation of tunnel boom noise



© Sebastian Terfloth

Student : Antoine Collier (01145967)
Supervisor : Dr. Joaquim Peiró

Department of Aeronautics
Imperial College London
South Kensington Campus
London SW7 2AZ
United Kingdom

October 8, 2016

Abstract

This project explore the application of the Kirchhoff and Ffowcs-Williams Hawkins (FWH) equations to the simulation of tunnel booms. A comparison between the two equations and their frequency response is made, revealing that they are sensitive to high frequencies and that the Kirchhoff model is for some terms a linearised version of the FWH model. These models require information on the air flow at the exit portal of the tunnel. A discontinuous Galerkin method, after calibration on experimental data, is used to simulate these flow information. The simulated micro-pressure wave at the exit portal does not exactly corresponds to the experimental data. An investigation into the approximations made reveals that the observation point is not far enough from the portal for the integrals of the models to be approximated by a multiplication. Except for a noticeable time shift, our simulation is then in better agreement with the experimental data. Numerically induced oscillations are also investigated. Finally, the influence of the shape of the train nose, the length of the nose, the train speed and the blockage ratio on the micro-pressure wave is studied, leading to advices on how to reduce the tunnel boom noise.

Acknowledgements

I would like to thank here Dr. Peiró for his advices during this project and his patience.

Table of Contents

1	Introduction	1
2	Discontinuous Galerkin Model	1
3	Calibration of the Discontinuous Galerkin method	4
4	Physical phenomena in the tunnel and the radiated micro-pressure wave	6
5	Modelisation and simulation of the micro-pressure wave	7
5.1	Kirchhoff and Ffowcs-Williams Hawkins models	7
5.2	Sensitivity of the two models to high frequencies	8
5.3	Evaluating p' , ρ , u and their derivatives	10
5.4	Validation of the kirchhoff and FWH models	12
5.5	Comparison of both models	14
6	Numerically induced errors	17
6.1	Influence of the mesh size on numerical oscillations	17
6.2	Influence of the nose shape on numerical oscillations	18
6.3	Investigation on the integral aproximation error	20
7	Parametric study of the micro-pressure wave	22
7.1	Influence of the length of the nose	22
7.2	Influence of the blockage ratio	24
7.3	Influence of the train speed	25
8	Conclusion	27

List of Figures

3.1	Pressure fluctuation p' history at $x=1.828\text{m}$	5
3.2	Pressure fluctuation p' history at $x=7.227\text{m}$	5
4.1	Variations of $\Delta p'$ in the x - t plane	6
5.1	Tunnel exit portal model with ground reflexion, adapted from [1]	7
5.2	Frequency response of the Kirchhoff model	9
5.3	Comparison of $\frac{\partial p}{\partial x}$ history at the exit portal obtained with each method for 200 cells	11
5.4	Comparison of $\frac{\partial p}{\partial x}$ history at the exit portal obtained with each method for 1500 cells	11
5.5	Comparison of $\frac{\partial(\rho u)}{\partial t}$ history at the exit portal obtained with each method for 200 cells	12
5.6	FFT of $\frac{\partial(\rho u)}{\partial t}$ history at the exit portal obtained with each method for 200 cells	12
5.7	Pressure history obtained with the two models near the exit portal for 300 cells	13
5.8	Zoom on A	13
5.9	Zoom on B	13
5.10	Zoom on C	13
5.11	Comparison of p' with models and experimental data at observation point for 200 cells	14
5.12	Sound level of both model and experimental data at the tunnel exit	15
5.13	Comparison of p' with models and experimental data at observation point for 200 cells	15
5.14	Influence of the mesh size on the pressure fluctuations given by the Kirchhoff model	16
5.15	FFT comparing the influence of mesh size on the Kirchhoff model	16
6.1	Influence of the mesh size on the pressure fluctuations given by the Kirchhoff model	17
6.2	FFT comparing the influence of mesh size on the Kirchhoff model	17
6.3	Illustration of a cosine tail shape for the model	18
6.4	Illustration of a linear tail shape for the model	18
6.5	Exit pressure fluctuations comparison for cosine and tail shape (200 cells) .	18
6.6	FFT comparison of exit pressure fluctuations for cosine and tail shape (200 cells)	18
6.7	Exit pressure fluctuations comparison for cosine and tail shape (700 cells) .	19
6.8	FFT comparison of exit pressure fluctuations for cosine and tail shape (700 cells)	19
6.9	Exit pressure fluctuations comparison for cosine and tail shape (1500 cells)	19
6.10	FFT comparison of exit pressure fluctuations for cosine and tail shape (1500 cells)	19

6.11	Comparison of Kirchhoff model for integral approximation and numerical integral (450 cells)	20
7.1	Influence of L_n on the micro-pressure wave shape	22
7.2	Spatial evolution of p inside the tunnel for L_n varying, at $t = 0.06s$	23
7.3	Pressure history inside the tunnel at $x = 7.227m$ for L_n varying	23
7.4	Variation of the amplitude of the micro-pressure wave with L_n	23
7.5	Influence of β on the micro-pressure wave shape	24
7.6	Spatial evolution of p inside the tunnel for β varying, at $t = 0.06s$	24
7.7	Pressure history inside the tunnel at $x = 7.227m$ for β varying	24
7.8	Variation of the amplitude of the micro-pressure wave with β	25
7.9	Influence of the v_{Tr} on the micro-pressure wave shape	25
7.10	Pressure history inside the tunnel at $x = 7.227m$ for V_{Tr} varying	25
7.11	Variation of the amplitude of the micro-pressure wave with v_{Tr}	26

1 Introduction

Tunnel boom is an acoustic phenomenon occurring when a train enters at high speed into a tunnel. It appeared with the development of ever faster trains, today reaching mean design speeds of 200 km/h to 300 km/h. This tunnel boom is a noise pollution for populations living near the tunnel, and as such has to be modeled to help designing noise free tunnels.

In order to simulate the tunnel boom, we need to get access to different properties of the flow. Since a direct numerical simulation is heavy in computation time, we seek a different approach. We will combine a discontinuous Galerkin method with two noise models, the Kirchhoff and the Ffowcs Williams Hawkings equations. We will then try to validate our model using an experimental dataset, investigate on our assumptions and our models, and see how the tunnel and train parameters can affect the tunnel boom noise.

2 Discontinuous Galerkin Model

We use a program written in C implementing a discontinuous Galerkin numerical method [2] to solve the following 1D equations of conservation (mass, momentum and energy) for compressible flows in the tunnel

$$\frac{\partial \mathbf{U}}{\partial t} + \frac{\partial \mathbf{F}(\mathbf{U})}{\partial x} = \mathbf{S} \quad (2.1)$$

with

$$\begin{aligned} \mathbf{U} = \check{\mathbf{U}}A = \begin{bmatrix} \rho \\ \rho u \\ \rho E \end{bmatrix} A; \quad \mathbf{F}(\mathbf{U}) = \check{\mathbf{F}}(\check{\mathbf{U}})A = \begin{bmatrix} \rho u \\ (\rho u^2 + p) \\ \rho u H \end{bmatrix} A; \\ \mathbf{S} = \check{\mathbf{S}}_1 \frac{\partial A}{\partial x} + \check{\mathbf{S}}_2 + \check{\mathbf{S}}_3 \frac{\partial A}{\partial x} = \begin{bmatrix} 0 \\ p \\ 0 \end{bmatrix} \frac{\partial A}{\partial x} + \begin{bmatrix} 0 \\ D_m \\ D_h \end{bmatrix} + \begin{bmatrix} 0 \\ p C_c \\ -V C_c \end{bmatrix} \frac{\partial A}{\partial x} \end{aligned} \quad (2.2)$$

where ρ is the fluid density, A is the cross-sectional area of the tunnel, p and u are the pressure and velocity fields in the tunnel, e is the internal energy of the fluid per unit mass, and $E = e + \frac{1}{2}u^2$ and $H = E + \frac{p}{\rho}$ respectively the total energy and total enthalpy per unit mass.

The presence of the train in the tunnel is modeled by the variation of the cross-sectional area A , which has been separated from the different terms to avoid oscillations due to projection of the moving area on the 1D grid [2]. The presence of a changing cross-sectional area A is responsible for the first term of the source \mathbf{S} . We account for the dissipation of momentum D_m and enthalpy D_h due to the friction of the flow on the train and tunnel walls. The 3D parts of the flow generated by the tail and the nose of the train are also accounted with the momentum $Q_m = pC_c \frac{\partial A}{\partial x}$ and enthalpy $Q_h = -VC_c \frac{\partial A}{\partial x}$ corrections terms. The coefficient C_c is dependent upon the train speed and its geometry.

By multiplying the equation (2.1) by a test function w , integrating it over the whole domain Ω of N non-overlapping mesh elements Ω_e such that $\Omega = \cup_{e=1}^N \Omega_e$, and assuming a piece-wise elemental approximation we get

$$\int_{\Omega_e} w \frac{\partial \mathbf{U}}{\partial t} dx + \int_{\Omega_e} w \frac{\partial \mathbf{F}(\mathbf{U})}{\partial x} dx = \int_{\Omega_e} w \mathbf{S}(\mathbf{U}) dx \quad (2.3)$$

After an integration by parts of the flux term and using equation (2.2) we get

$$\begin{aligned} \int_{\Omega_e} w \frac{\partial \check{\mathbf{U}}}{\partial t} A dx + \int_{\Omega_e} w \check{\mathbf{U}} \frac{\partial A}{\partial t} dx - \int_{\Omega_e} \frac{dw}{dt} \check{\mathbf{F}}(\check{\mathbf{U}}) A dx + [w \check{\mathbf{F}}^u A]_{x_e^l}^{x_e^r} = \\ \int_{\Omega_e} w (\check{\mathbf{S}}_1(\check{\mathbf{U}}) + (\check{\mathbf{S}}_2(\check{\mathbf{U}}) + \check{\mathbf{S}}_1(\check{\mathbf{U}}) \frac{\partial A}{\partial x}) dx \end{aligned} \quad (2.4)$$

where x_e^l and x_e^r are the position of the left and right boundaries of the element Ω_e and $\check{\mathbf{F}}^u$ is the upwind numerical flux which links the discontinuous solution $\check{\mathbf{U}}$ between the elements.

Taking the projection of each of the terms of equation (2.4) on the Legendre polynomial basis of dimension $P + 1$ and maximum polynomial degree P we get

$$\begin{aligned} \check{\mathbf{U}}|_{\Omega_e}(x_e(\xi), t) &= \sum_{p=0}^P L_p(\xi) \bar{\mathbf{U}}_p(t) \\ \check{\mathbf{F}}(\check{\mathbf{U}}|_{\Omega_e}(x_e(\xi), t)) &= \sum_{p=0}^P L_p(\xi) \bar{\mathbf{F}}_p(t) \\ \check{\mathbf{S}}_i(\check{\mathbf{U}}|_{\Omega_e}(x_e(\xi), t)) &= \sum_{p=0}^P L_p(\xi) \bar{\mathbf{S}}_{i,p}(t) \quad i \in [1; 3] \end{aligned} \quad (2.5)$$

with $\xi \in [-1; 1]$ on the reference element Ω_e . Considering that Legendre polynomials are orthogonal, we choose a test function $w|_{\Omega_e}(x_e(\xi)) = L_q(\xi)$ with $q \in [0; P]$. The equation (2.4) can now be written

$$\mathcal{M}_A \frac{d\bar{\mathbf{U}}_p}{dt} + \mathcal{M}_{\partial A} \bar{\mathbf{U}}_p - \mathcal{D}_A \bar{\mathbf{F}}_p + [L_q(\xi) \check{\mathbf{F}}^u A(\xi, t)]_{x_e^l}^{x_e^r} - \mathcal{M}_A \bar{\mathbf{S}}_{2,p} - \mathcal{M}_S (\bar{\mathbf{S}}_{1,p} + \bar{\mathbf{S}}_{3,p}) = 0 \quad (2.6)$$

where the matrices coefficients are

$$\begin{aligned}
\mathcal{M}_{Apq} &= \int_{-1}^1 L_q(\xi) L_p(\xi) A(\xi, t) d\xi \\
\mathcal{M}_{\partial Apq} &= \int_{-1}^1 L_q(\xi) L_p(\xi) \frac{\partial A(\xi, t)}{\partial t} d\xi \\
\mathcal{M}_{Spq} &= \int_{-1}^1 L_q(\xi) L_p(\xi) \frac{\partial A(\xi, t)}{d\xi} d\xi \\
\mathcal{D}_{Apq} &= \int_{-1}^1 \frac{dL_q(\xi)}{d\xi} L_p(\xi) A(\xi, t) d\xi
\end{aligned} \tag{2.7}$$

This equation can finally be rewritten (assuming \mathcal{M}_A is invertible)

$$\frac{d\bar{\mathbf{U}}_p}{dt} = \mathbf{R}(\bar{\mathbf{U}}_p, t) \tag{2.8}$$

Equation (2.8) is numerically solved using a Range-Kutta method, with each term being calculated at all time steps for all the domain. Stability of this scheme is ensured for a suited CFL number. One can note that the projection of \mathbf{U} , $\mathbf{F}(\mathbf{U})$ and $\mathbf{S}(\mathbf{U})$ on the Legendre polynomial space of degree P induces a loss of information, but is a good approximation with sufficiently small elements Ω_e and without many variations on Ω_e of those functions.

3 Calibration of the Discontinuous Galerkin method

Before using the data given by this model to try to simulate a tunnel boom, we need to ensure that it is able to reproduce pressure data acquired during some experiments. We use data from [1], an experiment conducted by the Netherlands Aerospace center (NLR) [3] for the Seoul National University.

The experiment has been conducted on a model scale tunnel, with a pneumatic launch system allowing to speed up to $500km/h$ a model train. Pressure transducers have been placed into the tunnel and microphones near the exit portal to record the pressure fluctuations due to the train. The relevant parameters of both the tunnel and the train used are summerized in the following tables:

Length	Shape	Cross Perimeter	Cross Area	Height	Width
$L_{Tu} = 7.64m$	<i>Rectangle</i>	$P_{Tu} = 274mm$	$A_{Tu} = 3880mm^2$	$h_{Tu} = 40mm$	$w_{Tu} = 97mm$

Table 3.1: Tunnel model relevant parameters

Length	Shape	Blockage Ratio	Diameter	Nose Length	Speed
$L_{Tr} = 2.34m$	<i>Bullet</i>	$\beta = 0.081$	$D_{Tr} = 20mm$	$L_n = 70mm$	$v_{Tr} = 300km/h$

Table 3.2: Train model relevant parameters

Four parameters needed for the simulation code input are missing: the train C_{fg} and tunnel C_{ft} friction coefficients and the nose C_{Dn} and tail C_{Dt} drag coefficients. These are critical parameters for the model. We use a cross-validation strategy to select them: firstly by fitting the simulated pressure history with the experimental data at the tunnel location $x = 1.228m$ (measured from the tunnel entrance), then validating the coefficients used with the experimental pressure history data at the tunnel location $x = 7.227m$.

Each coefficient has an effect on the simulated pressure history which can be explained as follows:

- Increasing the nose drag coefficient C_{Dn} increases the amplitude of the initial compression wave generated at the entry of the train nose in the tunnel, since it increases the wall-breaking effect of the train with a virtually less slender body.
- Increasing the tail drag coefficient C_{Dt} increases the amplitude of the initial expansion wave created by the entry of train tail in the tunnel, for the same reasons.
- Increasing the train friction coefficient C_{fg} increases the slope at which the pressure rises after the first jump since more air is set in motion through viscous effect by the train in the tunnel.

- Increasing the tunnel friction coefficient C_{ft} decreases the amplitude of the compressions and rarefactions wave through time as it works against the motion of the air in the tunnel and thus induces loss of energy during the pressure waves propagation.

Using these information, we can fit the simulation to the first experimental data set at $x = 1.828m$ from the tunnel entrance. Then we cross-validate the results at $x = 7.227m$. The simulation results are compared with the experimental results we try to reproduce from [1]. The time $t = 0s$ corresponds to the entry of the train into the tunnel.

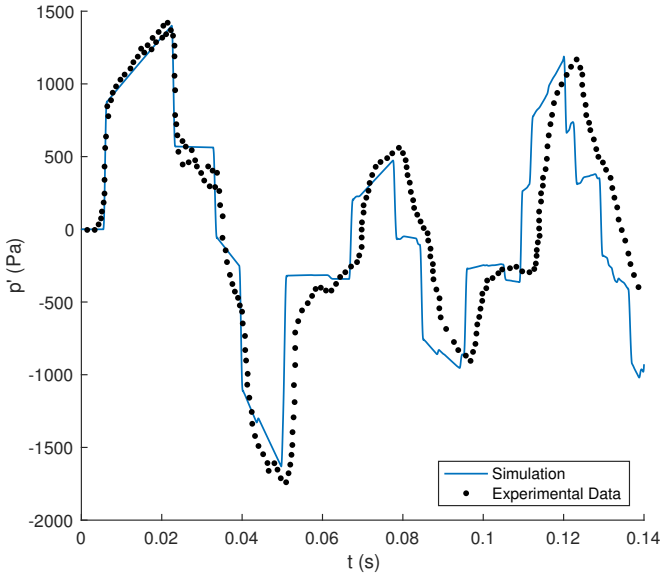


Figure 3.1: Pressure fluctuation p' history at $x=1.828m$

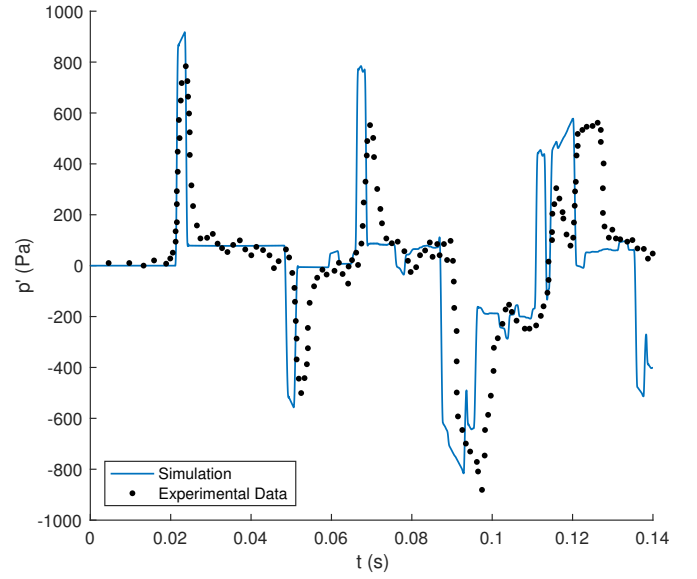


Figure 3.2: Pressure fluctuation p' history at $x=7.227m$

From the figures (3.1) and (3.2) we can see that our model does a great job at predicting the general shape of the pressure histories. Most peaks observed on the experimental data are present on our simulation results. We can though notice a slight time interval between the experimental and data spikes. This interval is increasing with time. A stark difference starting at $t = 0.0135s$ on (3.2) can be observed between our model and the experimental data. This might result from the time shift, the simulation probably already simulating what would happen after $t = 0.14s$ for the experimental data. As we do not have the experimental data after that time, we cannot verify this assumption. We can also notice that most variations of pressure are smoother on the experimental data than on our simulation.

The selection of our input simulation parameters could explain the dissimilarities between the shape of our simulated curves and the experiment. For instance the shape of the nose of the train is an axi-symmetric bullet for the experiment and a cosine (6.3) in our simulation. The 4 coefficients we calibrated might not be a perfect combination as well. Still, the initial compression wave, which creates the tunnel boom, is well modeled. We thus use our program to simulate the impact on the flow of a train going through a tunnel at high speed.

4 Physical phenomena in the tunnel and the radiated micro-pressure wave

Before the entry of the train in the tunnel, the air is at rest. The train will hit this wall of air as it enters the tunnel, setting the air in motion and especially creating a compression wave. This compression wave will travel at the speed of sound inside the tunnel. When arriving on the tunnel exit, a part of this compression wave gets reflected back into the tunnel as a rarefaction wave while a part is transmitted outside the tunnel. The transmitted part generates the micro-pressure wave we want to simulate. The reflected part will continue its journey inside the tunnel. When hitting the entry portal of the tunnel or the nose and tail of the train, the same phenomenon will occur. The wave will lose its energy due to friction on the train and the walls until it dissipates entirely. The rarefaction wave created by the train tail entry in the tunnel behaves similarly. This results in a complex pattern of pressure variation inside the tunnel, as can be seen on figure (4.1).

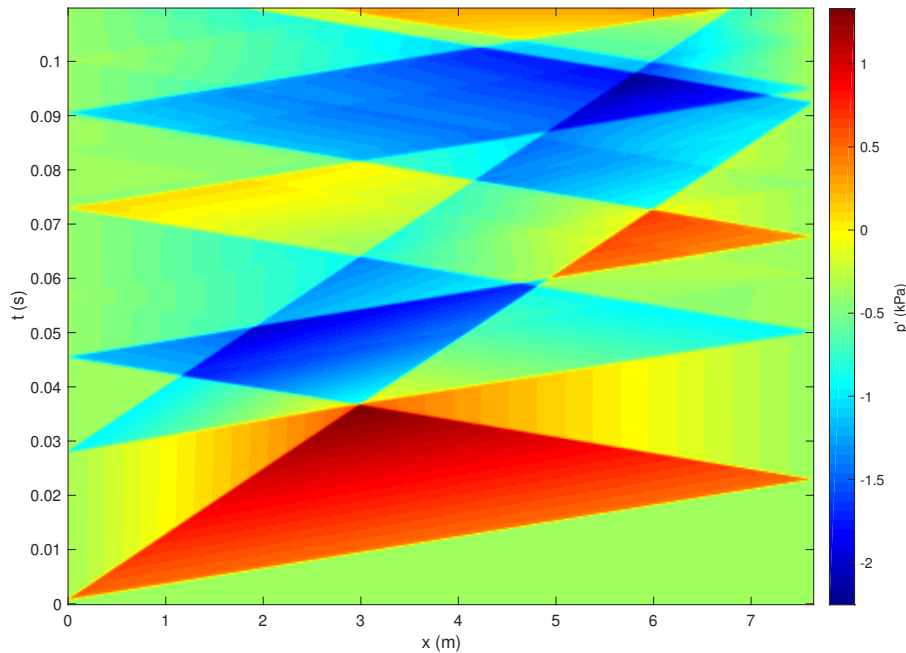


Figure 4.1: Variations of $\Delta p'$ in the x-t plane

The tunnel geometry has an impact on the travelling waves. Ballast tracks can dampen the pressure wave, and thus the amplitude of the tunnel boom, through porosity effects. The presence of ventilation shafts and emergency exits in the tunnel can also help relieving the pressure.

5 Modelisation and simulation of the micro-pressure wave

5.1 Kirchhoff and Ffowcs-Williams Hawkings models

Several models have already been used in the litterature to simulate the noise created at the exit portal of the tunnel by the transmitted micro-pressure wave. We propose to explore here two models: the Kirchhoff integral theorem (5.1), widely used in aeroacoustics [4], and the Ffowcs-Williams Hawkings (FWH) model (5.2).

$$p'(\mathbf{x}, t) = \frac{1}{4\pi} \int_S \left\{ \frac{p' \cos \theta}{r^2} + \frac{\partial p' \cos \theta}{\partial \tau \frac{cr}}{r} - \frac{1}{r} \frac{\partial p'}{\partial n} \right\}_{\tau, \mathbf{x}'} dS \quad (5.1)$$

$$p'(\mathbf{x}, t) = \frac{1}{4\pi} \int_S \left\{ \frac{p' \cos \theta}{r^2} + \frac{\partial p' \cos \theta}{\partial \tau \frac{cr}}{r} + \frac{1}{r} \frac{\partial(\rho u)}{\partial \tau} + \frac{\cos \theta}{cr} \frac{\partial(\rho u^2)}{\partial \tau} + \rho u^2 \frac{\cos \theta}{r^2} \right\}_{\tau, \mathbf{x}'} dS \quad (5.2)$$

In both models, the brackets means that the integral is evaluated at the retarded time $\tau = t - \frac{r}{c}$ with $r = \|\mathbf{r}\|$, $\mathbf{r} = \mathbf{x} - \mathbf{x}'$ being the radiation vector between the evaluation point \mathbf{x} and the integration point \mathbf{x}' and with c the speed of sound. θ is the angle between the unit normal \mathbf{n} of the closed integration surface S and the radiation vector \mathbf{r} . Finally p' is the pressure fluctuation. However, while the Kirchhoff model only uses 3 terms based on the pressure fluctuation and its derivatives, the FWH model also needs as an input the density and speed of the flow and their derivatives. The differences between the model will be explicated later on.

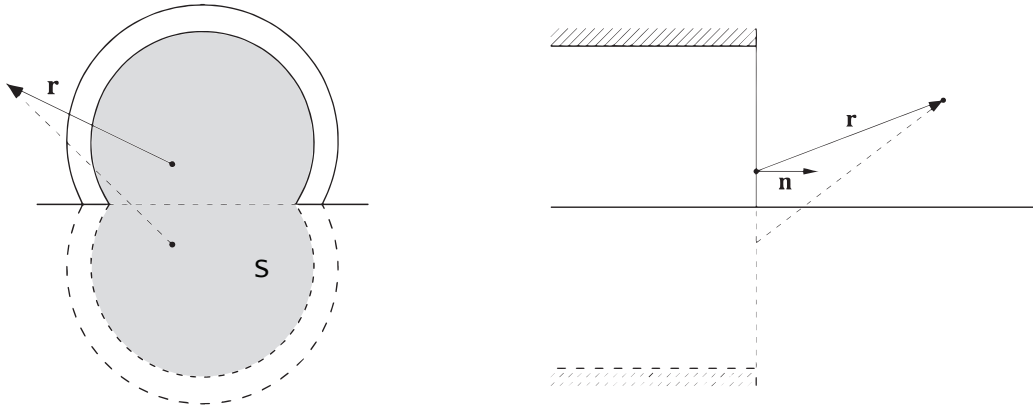


Figure 5.1: Tunnel exit portal model with ground reflexion, adapted from [1]

The reflexion of the incoming pressure waves on the slabs of the tunnel is accounted in our model by taking a symmetric tunnel exit portal on which to perform the integration.

Perfect reflexion is assumed. We also assume that far from the tunnel exit the pressure fluctuation and thus the speed of the flow are zero. By choosing the right closed integration surface S , this allows us to approximate both models to an integration on the exit portal of the tunnel only. Since we use a 1D code, all our flow parameters are constant at the exit-portal. For an observation point far enough from the tunnel exit, we can approximate the integral in both equations to a multiplication. This saves us computational time. In the end both models look like the following, with the factor 2 accounting for the symmetry:

$$p'(\mathbf{x}, t) = \frac{2A_{Tu}}{4\pi} \left\{ \frac{p' \cos \theta}{r^2} + \frac{\partial p' \cos \theta}{\partial \tau \frac{cr}{r}} - \frac{1}{r} \frac{\partial p'}{\partial n} \right\}_{\tau, \mathbf{x}'} \quad (5.3)$$

$$p'(\mathbf{x}, t) = \frac{2A_{Tu}}{4\pi} \left\{ \frac{p' \cos \theta}{r^2} + \frac{\partial p' \cos \theta}{\partial \tau \frac{cr}{r}} + \frac{1}{r} \frac{\partial(\rho u)}{\partial \tau} + \frac{\cos \theta}{cr} \frac{\partial(\rho u^2)}{\partial \tau} + \rho u^2 \frac{\cos \theta}{r^2} \right\}_{\tau, \mathbf{x}'} \quad (5.4)$$

5.2 Sensitivity of the two models to high frequencies

We can derive the analytical expression of the frequency response of both models to see how they behave. This is of interest, first of all to compare how the two models differ, but also because our numerical scheme introduces oscillations, which could be amplified by both Kirchhoff and FWH models.

$$\frac{\partial^2 p'}{\partial t^2} = c_0^2 \frac{\partial^2 p'}{\partial x^2} \quad (5.5)$$

To obtain the analytical frequency response of both model, we will use the fluctuations created by a 1D monochromatic acoustic plane wave. A solution p' to the 1D wave equations (5.5) travelling in the positive direction in our coordinates reference system can be seen on equation (5.6), using the complex variable \underline{p}' , with k the wave number and w the angular frequency of the wave. The pressure fluctuation at the exit portal being also a solution of the wave equation (5.5), it can be decomposed into a sum of simple sinusoidal oscillations, making valid the frequency analysis we are about to make.

$$p'(x, t) = \text{Re}(\underline{p}') = \text{Re}(Ae^{i(wt-kx)}) \quad (5.6)$$

The sound speed is defined as $c_0^2 = \frac{\partial p}{\partial \rho}|_s$. Assuming the movement of the sound waves in the fluid is an isentropic process we get the equation (5.7) linking the pressure fluctuations p' and density fluctuations ρ' .

$$\rho' = \frac{p'}{c_0^2} \quad (5.7)$$

From the linearised continuity equation and neglecting the density fluctuations ρ' compared to the mean density ρ_0 we can obtain an expression linking p' to the speed of air fluctuations u' .

$$\frac{\partial u'}{\partial x} = -\frac{1}{\rho_0} \frac{\partial \rho'}{\partial t} \quad (5.8)$$

which, after using equation (5.7) and transforming the time derivative of the pressure by a spatial derivative, gives equation (5.9).

$$u' = \frac{p'}{\rho_0 c_0} \quad (5.9)$$

Using complex variables we can thus derive the values of the derivatives needed for both models.

$$\begin{aligned} \frac{\partial \underline{p}'}{\partial t} &= i\omega \underline{p}' \\ \frac{\partial \underline{p}'}{\partial x} &= -ik \underline{p}' \\ \frac{\partial(\rho \underline{u}')}{\partial t} &= \frac{\partial(\rho_0 + \rho') \underline{u}'}{\partial t} = \frac{i\omega}{c_0} \underline{p}' + \frac{2i\omega}{\rho_0 c_0^3} \underline{p}'^2 \\ \frac{\partial(\rho \underline{u}'^2)}{\partial t} &= \frac{2i\omega}{\rho_0 c_0^2} \underline{p}'^2 + \frac{3i\omega}{\rho_0^2 c_0^4} \underline{p}'^3 \end{aligned} \quad (5.10)$$

Using expressions from equation (5.10), we can get the frequency response from the Kirchhoff model (5.11) and FWH model (5.12). We can note that the phase change $\phi = e^{-i\frac{\omega r}{c_0}}$ induced by the retarded time evaluation does not make any difference on the amplitude of the models, but is still shown for the sake of clarity.

$$H = \frac{|p'_{kirchhoff}(x, t)|}{|p'_{portal}(x, t)|} = \frac{2A_{Tu}}{4\pi} \sqrt{\left(\frac{\cos\theta}{r^2}\right)^2 + \left(\frac{\omega}{cr}(\cos\theta + 1)\right)^2} |e^{-i\frac{\omega r}{c_0}}| \quad (5.11)$$

$$\underline{p}'_{FWH} = \frac{2A_{Tu} e^{-i\frac{\omega r}{c_0}}}{4\pi} \left[\left(\frac{\cos\theta}{r^2} + \frac{i\omega(\cos\theta + 1)}{c_0 r}\right) \underline{p}' + \frac{2i\omega(\cos\theta + 1)}{\rho_0 c_0^3 r} \underline{p}'^2 + \frac{\cos\theta}{r^2 \rho_0^2 c_0^4} \left(1 + \frac{3i\omega r}{c_0}\right) \underline{p}'^3 \right] \quad (5.12)$$

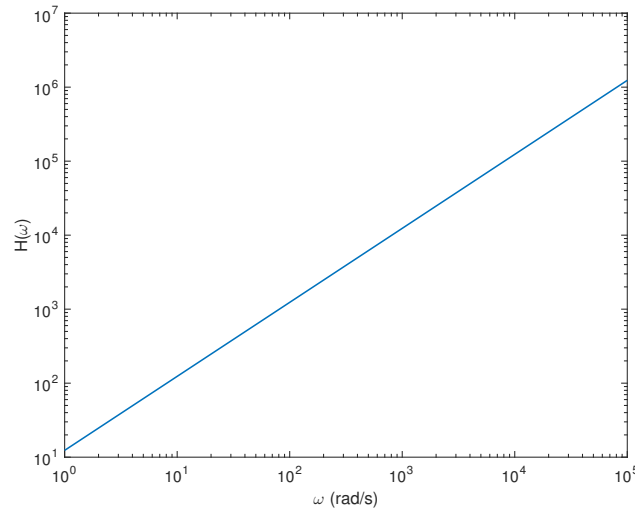


Figure 5.2: Frequency response of the Kirchhoff model

The linear frequency response of the Kirchhoff model shown on figure (5.2) confirms that this model is very sensitive to high frequencies and thus oscillations. This is in the end expected as there are derivatives in its expression (5.1). This means that we must seek to minimize the existence of high frequency numerically induced oscillations in our simulation.

The expression of the FWH frequency response (5.12) being *non-linear*, we cannot derive a transfer function as we did for the Kirchhoff model. Still, the presence of ω as a multiplier confirms that this model is as well sensitive to high frequencies.

5.3 Evaluating p' , ρ , u and their derivatives

In order to use the two models with our simulation program, we need to get access to ρ , p' , u and their derivatives at the tunnel exit. The program gives us access to the Legendre approximation of

$$\check{\mathbf{U}} = \begin{bmatrix} \rho \\ \rho u \\ \rho E \end{bmatrix} \quad (5.13)$$

and since $p = (\gamma - 1)\rho(E - \frac{1}{2}u^2)$ to the primitive variables

$$\begin{bmatrix} \rho \\ u \\ p \end{bmatrix} = \begin{bmatrix} \check{U}_0 \\ \check{U}_1/\check{U}_0 \\ (\gamma - 1)(\check{U}_2 - \frac{1}{2}\check{U}_0\check{U}_1) \end{bmatrix} \quad (5.14)$$

From the very nature of the Discrete Galerkin model we use, we can access after each Range-Kutta step applied on equation (2.8) to the time derivatives of the Legendre approximation of $\check{\mathbf{U}}$, which can be reconstructed from $\bar{\mathbf{R}}$. Using the formula of the derivative of a product of functions we can retrieve all derivatives needed for both Kirchhoff and FWH models:

$$\frac{\partial(\rho u)}{\partial t} = R_1, \quad \frac{\partial(\rho u^2)}{\partial t} = u(2R_1 - uR_0), \quad \frac{\partial p}{\partial t} = (\gamma - 1)(R_2 - \frac{1}{2}u(2R_1 - uR_0)) \quad (5.15)$$

The spatial derivative of the pressure can also be obtained directly from our model since we have from equation (2.5) that the spatial derivatives of all components of $\check{\mathbf{U}}$ can be evaluated as

$$\frac{\partial \check{\mathbf{U}}|_{\Omega_e}(x_e(\xi), t)}{\partial x} = \sum_{p=0}^P \frac{dL_p(\xi)}{d\xi} \bar{\mathbf{U}}_p(t) \quad (5.16)$$

which combined with $p = (\gamma - 1)(-\frac{1}{2}\frac{(\rho u)^2}{\rho})$ gives us

$$\frac{\partial p}{\partial x} = (\gamma - 1)\left(\frac{\partial(\rho E)}{\partial x} + \frac{1}{2}u^2\frac{\partial \rho}{\partial x} - u\frac{\partial(\rho u)}{\partial x}\right) \quad (5.17)$$

We seek to get the derivatives with the less numerically induced oscillations possible for a low computational cost. We will compare the results obtained with this direct method with finite differences. First and second order backward finite differences for first

derivative have thus been implemented in the code. An implementation of the Legendre reconstruction of $\check{\mathbf{R}}$ from the values of $\bar{\mathbf{R}}$ has been added, which was not previously available. The time-window chosen to compare the derivatives obtained with each method corresponds to the part generating the micro-pressure wave.

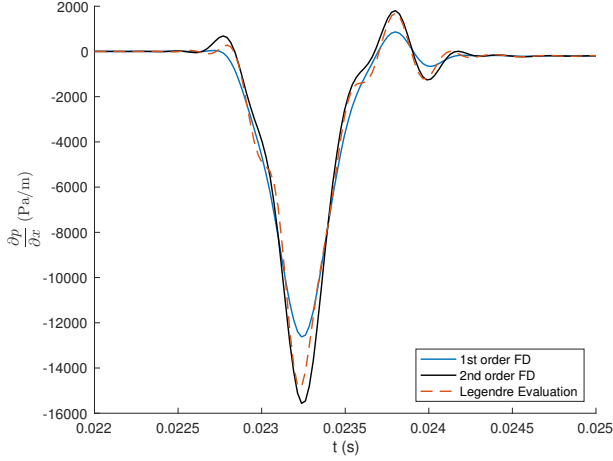


Figure 5.3: Comparison of $\frac{\partial p}{\partial x}$ history at the exit portal obtained with each method for 200 cells

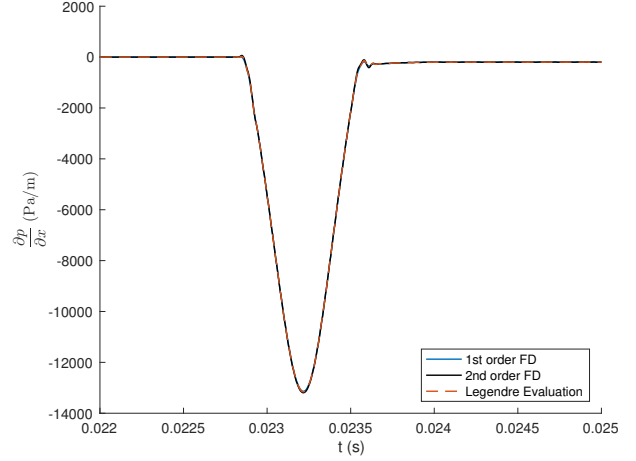


Figure 5.4: Comparison of $\frac{\partial p}{\partial x}$ history at the exit portal obtained with each method for 1500 cells

The Legendre evaluation of the derivatives are obtained from $\check{\mathbf{R}}$, an approximation of \mathbf{R} , and are thus as precise as the size of the elements Ω_e allows. Figure (5.3) allows us to see that for the spatial pressure gradient, the Legendre evaluation is more oscillatory for a low number of cells than both FD methods, and thus seem more prone to oscillations and less accurate than the finite differences. But an interesting point to notice is that finite differences, obtained from the values of \check{U} , are here an approximation of the derivatives obtained with Legendre evaluation through (5.15) and (5.17), and not of the exact derivatives. To be accurate, the Legendre evaluation should be taken. As figure (5.4) shows, all methods converge to the same values for a mesh large enough.

For the temporal gradients $\frac{\partial(\rho u)}{\partial t}$ and $\frac{\partial(\rho u^2)}{\partial t}$, there is a less clear difference between the three methods. This can be seen for $\frac{\partial(\rho u)}{\partial t}$ on figures (5.5) and (5.6).

The results obtained for $\frac{\partial p}{\partial t}$ were unexpected. It is far more oscillatory for the Legendre evaluation than for the FD methods, and the three methods did not have converged for a mesh size of 1500 cells. The only difference with the previous term in the Legendre method was the presence of the component \check{R}_2 of $\check{\mathbf{R}}$. This unexplained result could come from an error in the implementation of the Legendre evaluation realised for this work, even if the compatible results obtained for the other derivatives tend to say that there is no programming error.

Because of this seemingly wrong result for $\frac{\partial p}{\partial t}$ using Legendre evaluation, we will use for the calculation of the derivatives a second order Finite Differences method. One could argue that a higher order accurate scheme could have been better, but as we will see later, the second order FD already allows good accuracy for a small mesh size and is sufficient for the following study.

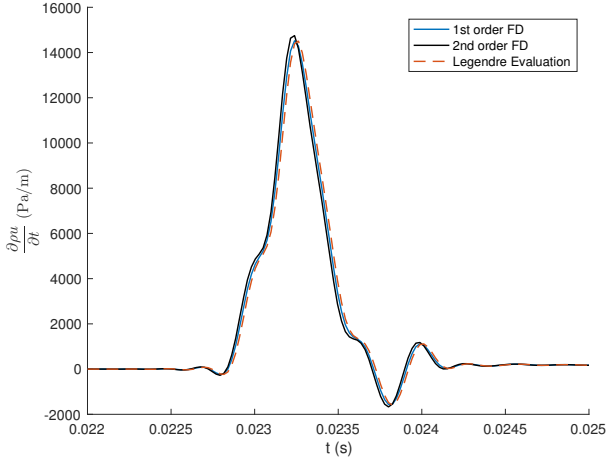


Figure 5.5: Comparison of $\frac{\partial(\rho u)}{\partial t}$ history at the exit portal obtained with each method for 200 cells

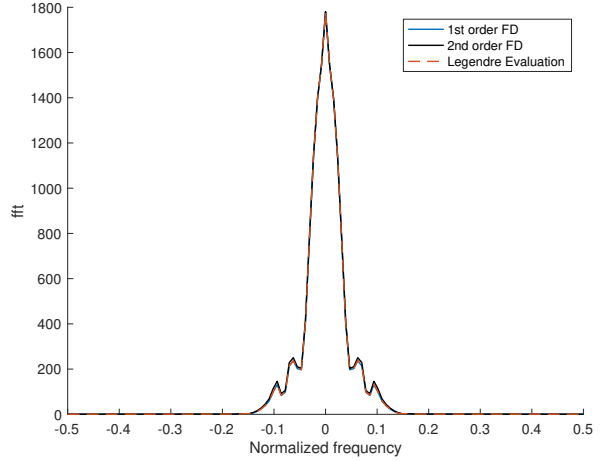


Figure 5.6: FFT of $\frac{\partial(\rho u)}{\partial t}$ history at the exit portal obtained with each method for 200 cells

5.4 Validation of the kirchhoff and FWH models

We now want to validate the use of Kirchhoff and Ffowcs-Williams Hawkins model to predict the tunnel boom. We use the noise data from the same NLR experiment [1] we used to calibrate the drag and friction coefficients. The data was obtained by placing a microphone near the tunnel exit, located 120mm from the exit portal plane, at 20mm above the ground and at 120mm from the tunnel axis. Through simple geometry, these information give us the corresponding r and θ values we need to plug in both Kirchhoff and FWH models. The pressure fluctuation and derivatives needed for the two models are taken from the code at the exit portal. The simulation parameters are chosen in accordance with the experiment parameters, at the exception of the nose shape. We do not have an axi-symmetric bullet nose shape in our program and thus use a cosine nose shape (6.3) in order to reduce the oscillations, as will be explained in chapter 6. Running the simulation for a numerical time of 0.14 seconds, we obtain near the exit portal the pressure fluctuations that can be seen on (5.7).

The pressure fluctuations history near the exit portal is mostly composed of spikes. The positive ones are due to the transmission through the exit portal of the initial compression wave generated by the train entry in the tunnel and its reflections, while the negative ones are due to the transmission of rarefaction waves. The first spike, located in zone A, is exactly at the same time location than the micro-pressure wave recorded during the NLR experiment. Though, we can see that there is a spike that is of higher amplitude in zone C. It corresponds to the exit from the tunnel of the tail of the train. The local tail rarefaction wave is transmitted into this positive spike. Since we do not have experimental data on this part of the experiment, we cannot conclude on the existence in reality of a micro-pressure wave of this amplitude. Our model might not be able to reproduce well the micro-pressure waves produced by the exit of the tail and nose of the train, since it must involve complex 3D effects of the flow. Our boundary condition $p' = 0$, which is in fact equivalent to the pressure waves hitting a wall rather than having a part being

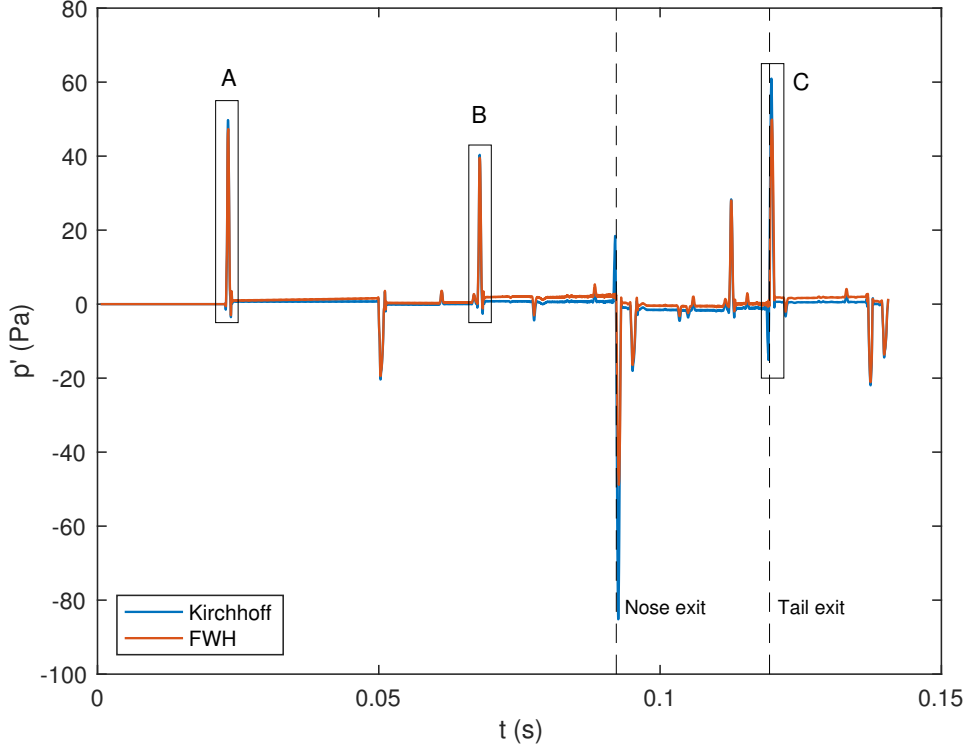


Figure 5.7: Pressure history obtained with the two models near the exit portal for 300 cells

transmitted into the atmosphere, might also be not compatible with the train exit. More data would be necessary to draw a conclusion. But we can compare the micro-pressure wave obtained in zone A with the experimental NLR data.

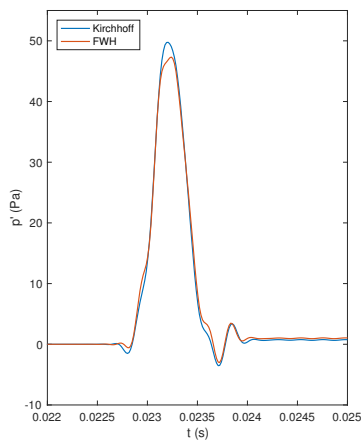


Figure 5.8: Zoom on A

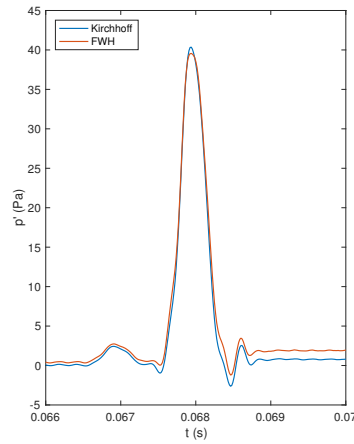


Figure 5.9: Zoom on B

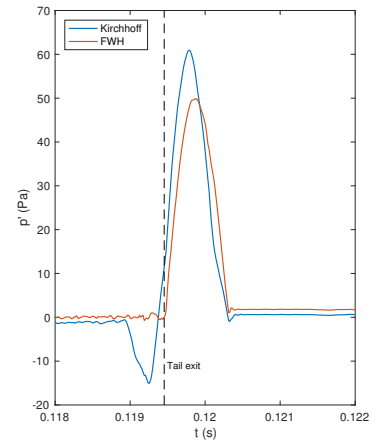


Figure 5.10: Zoom on C

Figure (5.11) allows us to get an insight on our ability to reproduce the experimental data from the NLR. We find approximately the same shape with the two models, with a pronounced spike and fluctuations of the pressure near zero before and after the pressure

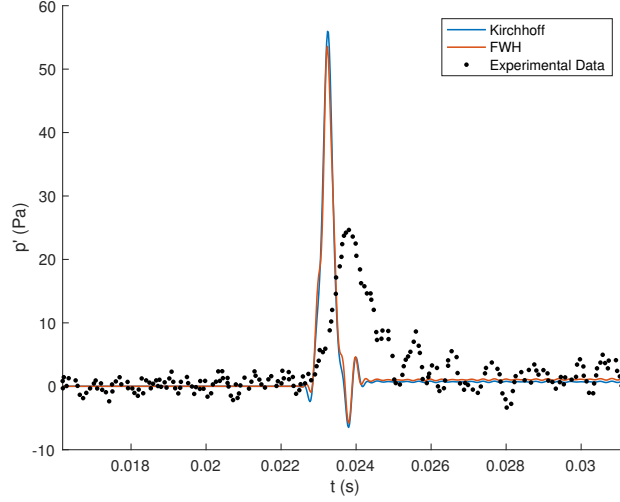


Figure 5.11: Comparison of p' with models and experimental data at observation point for 200 cells

spike. The time location of the start of the spikes is also compatible with the experimental data. Still, we can notice two not conclusive elements. The order of magnitude of our models, while compatible with the experimental data, is not as accurate as expected. There is also a noticeable difference in the time span of the micro-pressure wave between our models and the experiment.

The Sound Pressure Level (SPL) is given by equation (5.18). Our simulation results seem compatible with the micro-pressure wave phenomenon and with the experimental data which is supposed to be loud and disturbing. In fact, the threshold of pain of 130 dB has been stepped for our simulation, while the maximum SPL obtained with the experimental data is 121 dB . The noisy experimental data could explain the already high SPL before the micro-pressure wave.

$$SPL = 20 \log_{10} \left(\frac{p'_{rms}}{2 \cdot 10^{-5}} \right) \text{ with } p'_{rms} = \sqrt{p'^2} \quad (5.18)$$

With the current simulation settings we cannot reproduce the experimental data. In order to explain this, we will assess our model. Numerically induced errors will be assessed in chapter 6. The influence of the parameters of the problem will be assessed in chapter 7.

5.5 Comparison of both models

Before studying how the inputs of our models and our numerical scheme influence the pressure-wave, we will assess the differences between the Kirchhoff and the Ffowcs-Williams Hawkins models. As the analytic frequency response study using the linear acoustic theory already showed in equation (5.12), the FWH model is supposed to be more sensitive to high frequencies than the Kirchhoff model, due to the presence of the time derivatives $\frac{\partial(\rho u)}{\partial t}$ and $\frac{\partial(\rho u^2)}{\partial t}$. This observation can be backed by performing a FFT of the two models, showed on figure (5.13). The FFT amplitude is normalized to clearly show that the FWH

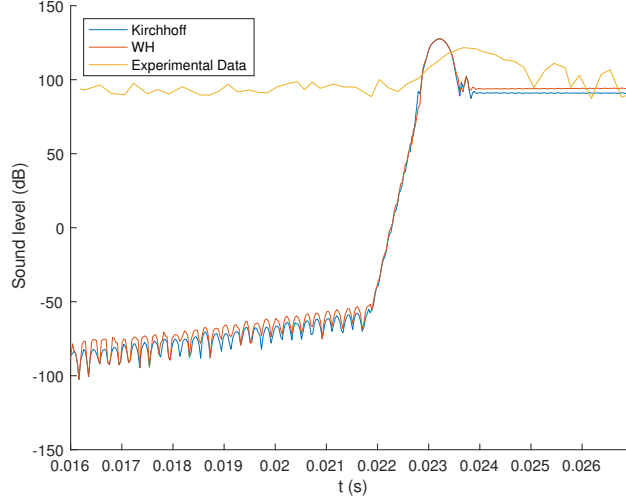


Figure 5.12: Sound level of both model and experimental data at the tunnel exit

has higher frequencies components than the Kirchhoff model, which is not obvious when not normalized.

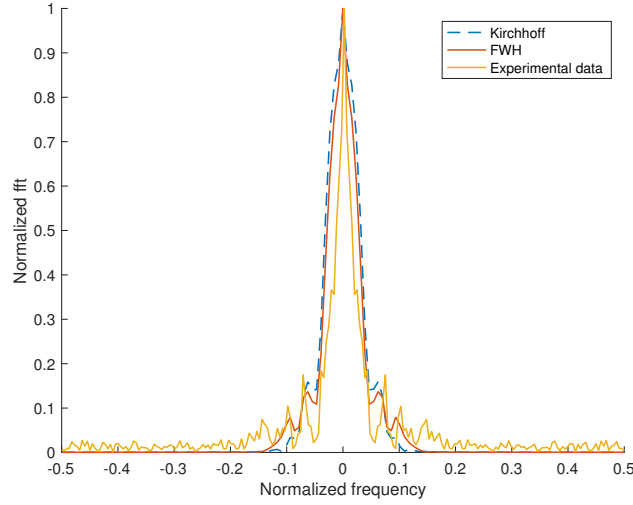


Figure 5.13: Comparison of p' with models and experimental data at observation point for 200 cells

We can also notice on figure (5.13) that the experimental data is more noisy than our numerical model. This can be explained by the low number of points of the experimental data, as well as the signal fluctuations of the microphones (the discrete error measured during the experiment was $\sim 1Pa$).

If we now perform a term by term comparison of the two models, we can see that each term does not have the same weight in the final expression. The terms are numbered in ascending order from left to right in equations (5.1) and (5.2).

The first two terms of the two models are identical. As can be seen on figure (5.14) those two terms have little to no impact on the shape and amplitude of the micro-pressure

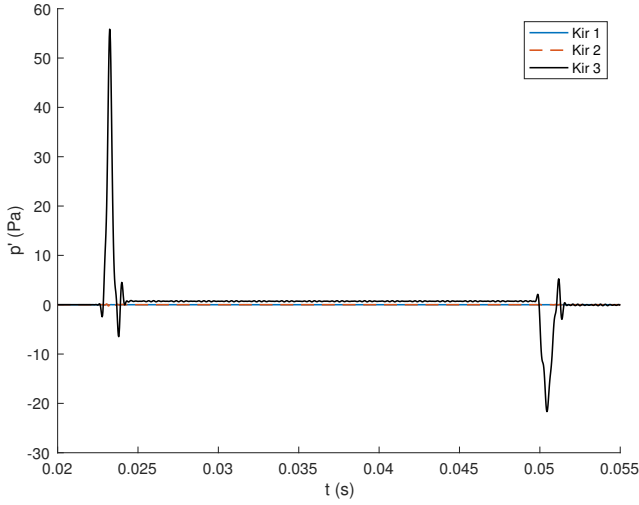


Figure 5.14: Influence of the mesh size on the pressure fluctuations given by the Kirchhoff model

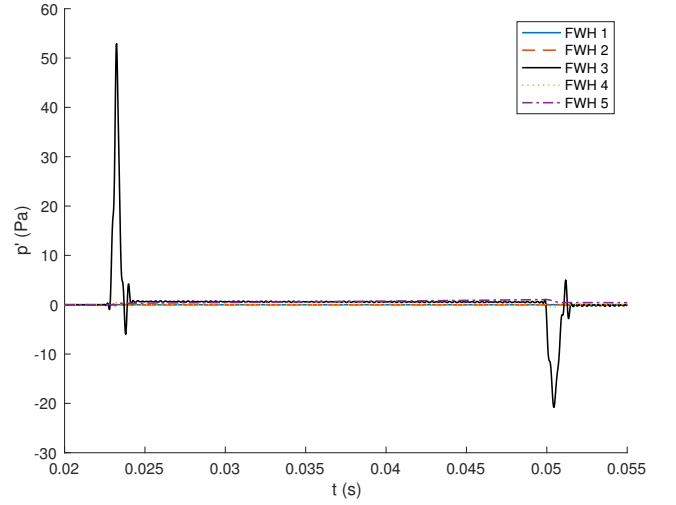


Figure 5.15: FFT comparing the influence of mesh size on the Kirchhoff model

wave. The dominant term in the Kirchhoff model is the spatial pressure gradient $\frac{\partial p}{\partial x}$. This is not a surprise and is a well established fact [1]. For the FWH model, the dominant term is the third one, linked to $\frac{\partial(\rho u)}{\partial t}$. It has the same shape than the pressure gradient in the Kirchhoff model. It is also not a surprise considering that from the conservation of momentum, neglecting viscosity and the density fluctuations ρ' compared to the mean density ρ_0 we get

$$\rho_0 \frac{\partial u}{\partial t} = -\frac{\partial p'}{\partial x} \quad (5.19)$$

Under these approximations, the third terms of the two models are equal. Finally, we can notice that the 5th term of the FWH model is not negligible and rises after each hit of a compression wave on the tunnel exit. It corresponds to a dynamic pressure. In the end, we can suppose that the Kirchhoff model is a linearised and simplified version of the FWH model, and that the FWH model is more accurate. This has been found in other studies [5].

6 Numerically induced errors

We constated in section 5.4 that our model was unable, with the current settings, to reproduce the experimental results of NLR. In this chapter we will assess the importance of numerical errors that could explain those results.

6.1 Influence of the mesh size on numerical oscillations

We want to confirm here that by increasing the number of cells, we can reduce the oscillations of both models. By reducing the size of the elements Ω_e , it is supposed to allow for the Legendre approximations of our flow parameters to be closer to the exact solutions.

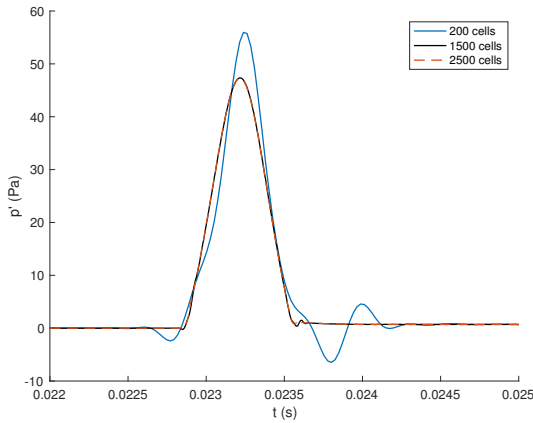


Figure 6.1: Influence of the mesh size on the pressure fluctuations given by the Kirchhoff model

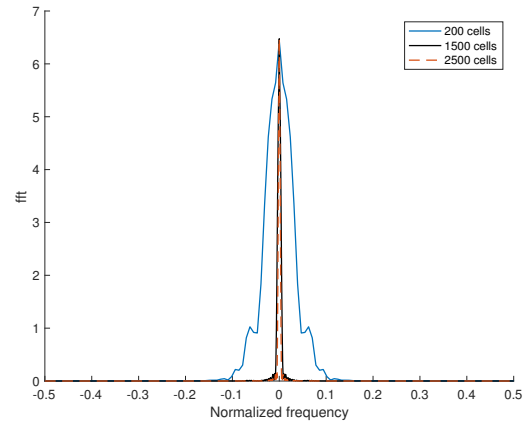


Figure 6.2: FFT comparing the influence of mesh size on the Kirchhoff model

Figure (6.1) allows to compare the influence of the number of elements in our mesh for the Kirchhoff model. Only one model is displayed for clarity, but the results are similar for the FWH model. There is a clear reduction of the oscillations in the vicinity of the spike as the mesh size is increased. This is confirmed by performing a FFT on the three simulation results (6.2). As one would expect, the size of our mesh is a determining factor for predicting the shape of the micro-pressure wave. We are limited with the high computational cost of using a detailed mesh.

6.2 Influence of the nose shape on numerical oscillations

The choice of a cosine shaped nose for the train is deliberate. While it is not a shape of nose used on real trains, it avoids the apparition of oscillations in our model. To confirm it, we run the simulation with a linear nose shape. The tail and nose shape we refer to are shown on figures (6.3) and (6.4). The cosine shape can be seen as a smoothed linear shape that allows the continuity of the tunnel area derivatives at the points colored in black.

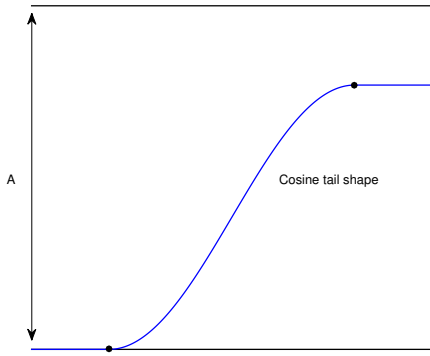


Figure 6.3: Illustration of a cosine tail shape for the model

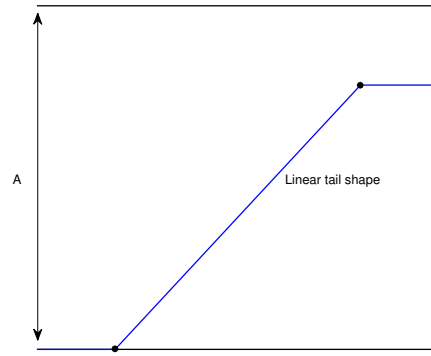


Figure 6.4: Illustration of a linear tail shape for the model

The results obtained with the Kirchhoff model near the exit portal with those two shape of nose and tails are shown on figures (6.5) and (6.6).

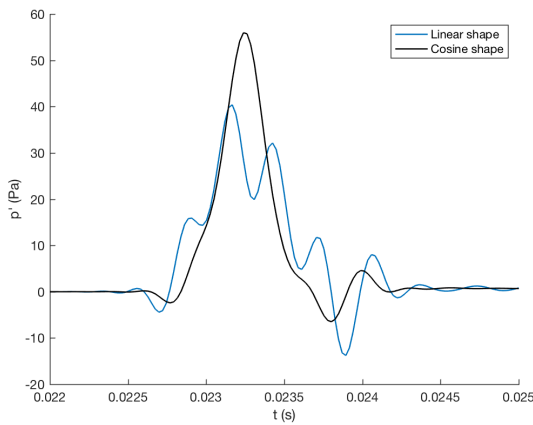


Figure 6.5: Exit pressure fluctuations comparison for cosine and tail shape (200 cells)

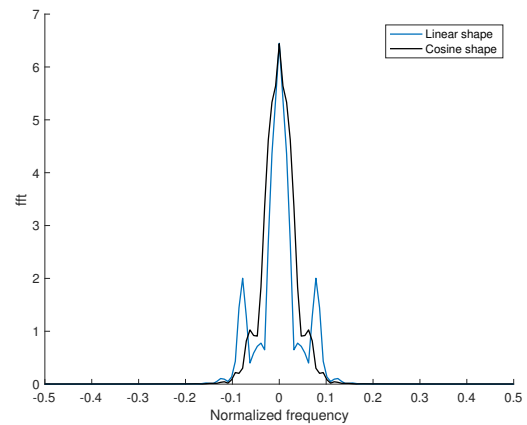


Figure 6.6: FFT comparison of exit pressure fluctuations for cosine and tail shape (200 cells)

We first see that the shape of the nose greatly influences the shape of the micro-pressure wave. Lots of oscillations are also induced by the linear nose shape. The presence of two distinct spikes on the FFT of the linear shape seem to indicate that they might be

numerically induced. If we increase the number of cells in our mesh, as seen on figure (6.7) and (6.8), we can see that the simulation with a linear shape has not converged and is in fact more oscillatory than before.

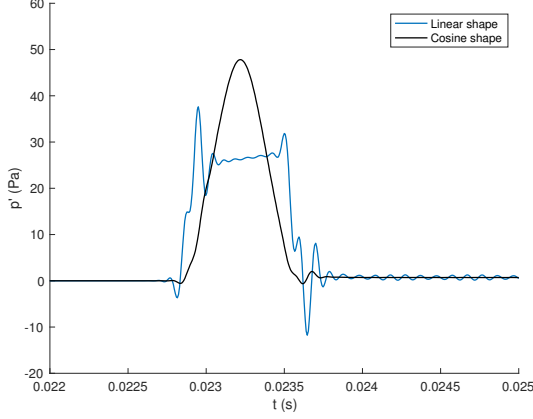


Figure 6.7: Exit pressure fluctuations comparison for cosine and tail shape (700 cells)

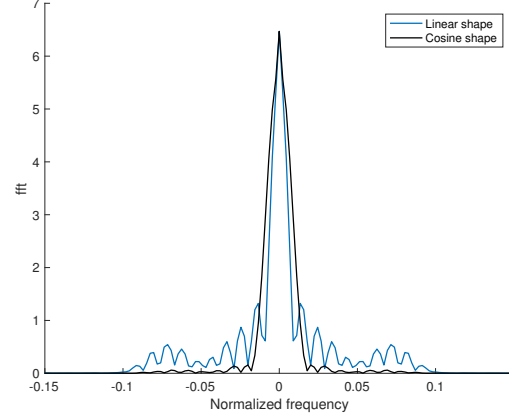


Figure 6.8: FFT comparison of exit pressure fluctuations for cosine and tail shape (700 cells)

If we again increase the number of cells in our mesh to 1500, figures (6.9) and (6.10), we can clearly see that the oscillatory behaviour of the linear nose and tail solution keeps increasing.

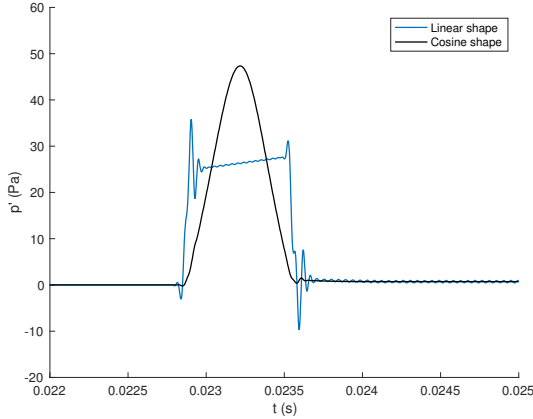


Figure 6.9: Exit pressure fluctuations comparison for cosine and tail shape (1500 cells)

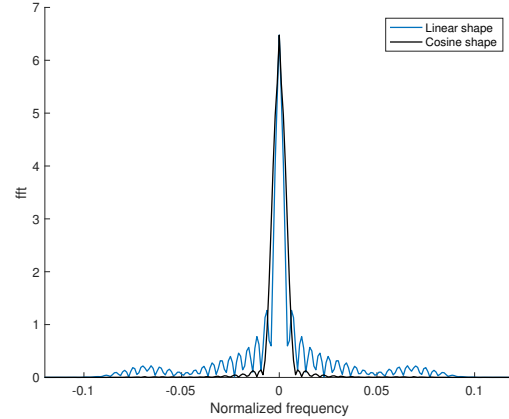


Figure 6.10: FFT comparison of exit pressure fluctuations for cosine and tail shape (1500 cells)

This could be explained by the presence in equation (2.2), on which our model has been based, of the term $\frac{\partial A}{\partial x}$. The discontinuous Galerkin approach we use is supposed to avoid such numerical oscillations due to discontinuities of area derivative. But this oscillatory behaviour, also observed on the other shape of nose with discontinuities, incriminate the discontinuity of the area. There are four critical points on which this derivative can be discontinuous, located at the beginning and end of both the nose and the tail of the train. Any numerical instant where one of the four critical points is located on the mesh will thus produce numerical oscillations. The more cells, the more likely the critical points to

be on the mesh during the simulation, and thus the more oscillations, explaining the non-converging curve of the linear shape. The choice of a smooth nose shape is thus critical to get smooth area derivatives and thus be able to predict the shape of the micro-pressure wave for a low computation cost.

6.3 Investigation on the integral approximation error

The integral approximation to a simple multiplication of both Kirchhoff and FWH models has been investigated to see if it could explain the stark difference of amplitude between our models results and the experimental data. The method used to evaluate the integral was a two dimensional Monte-Carlo. It is a really quick and easy way when vectorized to perform a numerical integration, with an error estimation. For a number of random point N $[x_i, y_i]$ large enough distributed over the integral surface $[a, b] \times [c, d]$, we have:

$$\int_a^b \left(\int_c^d f(x, y) dx \right) dy \approx (b - a)(d - c) \hat{f} \quad (6.1)$$

$$error \approx (b - a)(d - c) \sqrt{\frac{\hat{f}^2 - (\hat{f})^2}{N}}$$

with

$$\hat{f} = \frac{1}{N} \sum_{i=1}^N f(x_i, y_i), \quad \hat{f}^2 = \frac{1}{N} \sum_{i=1}^N f^2(x_i, y_i) \quad (6.2)$$

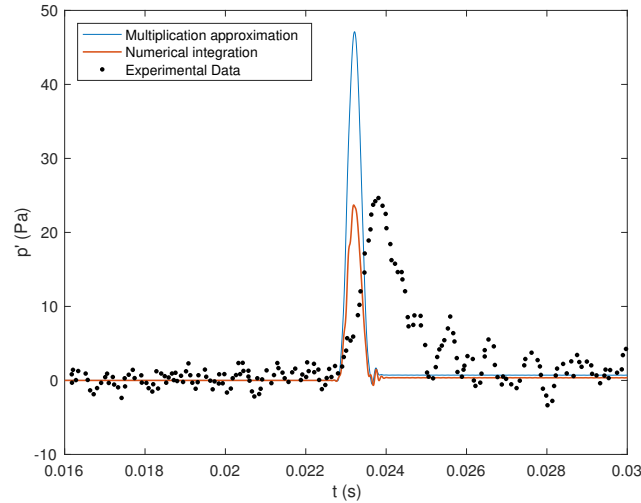


Figure 6.11: Comparison of Kirchhoff model for integral approximation and numerical integral (450 cells)

The numerically evaluated integral, for the same parameters as in the experiment can be seen on figure (6.11). 100000 random points were sufficient to observe convergence of the integral, the error on the integral value given being $\approx 0.1\%$. This proves that

the multiplication approximation of the integral used to perform quick evaluations of the Kirchhoff and FWH models creates an amplitude error of the micro-pressure wave of as much as 49%, and even if it saved computational time and was more facilitating, was not a good assumption. We now obtain a simulation that has nearly the same amplitude as the experimental data. The time shift between the experimental data and our simulation is still remaining.

7 Parametric study of the micro-pressure wave

We have seen that the Kirchhoff and FWH models, combined with our numerical tunnel simulation code, can give us a good estimate of the micro-pressure wave generated at the exit portal of a tunnel. The shape of the nose has proven to have a stark impact on the shape of the micro-pressure wave. We can study how other parameters of our model affect the micro-pressure wave.

Three parameters are investigated: the length of the nose of the train L_n , the speed of the train V_{Tr} and the blockage ratio β . We will again take a cosine shape to ensure the smoothness of the area, and reduce the apparition of numerically induced oscillations. As to not overcharge the figures, only the results obtained for the Kirchhoff model are shown. The results are indeed similar for the FWH model.

7.1 Influence of the length of the nose

We test here several length of train nose and their impact on the micro-pressure wave.

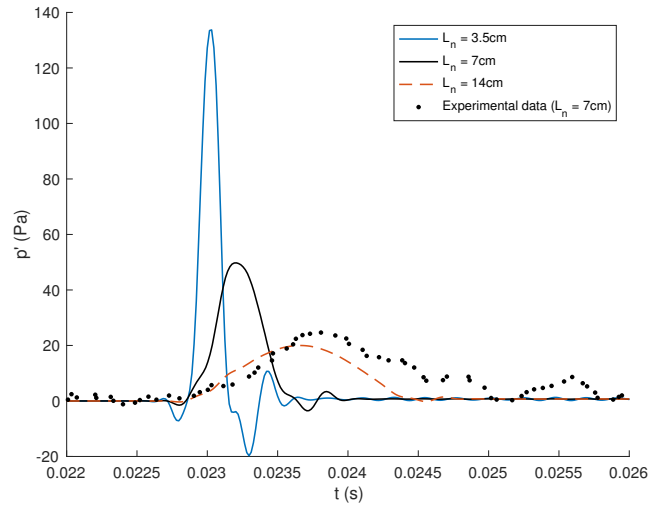


Figure 7.1: Influence of L_n on the micro-pressure wave shape

Figure (7.1) shows clearly that the longer the nose of the train, the smoother and the smaller in amplitude the micro-pressure wave. The creation of oscillations near the spike as already been discussed previously and are dependant on the mesh size. The creation of a bigger micro-pressure wave with a shorter nose can be explained by the creation of a higher intensity compression wave as the train enters the tunnel. We can see from the

first pressure jump on figure (7.3) that the longer the nose, the smoother the slope of the first pressure jump, and thus the smoother the pressure gradient will be at the exit portal leading to a decreased micro-pressure wave amplitude.

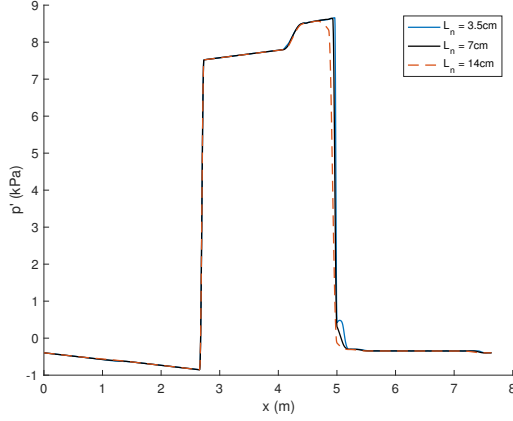


Figure 7.2: Spatial evolution of p inside the tunnel for L_n varying, at $t = 0.06s$

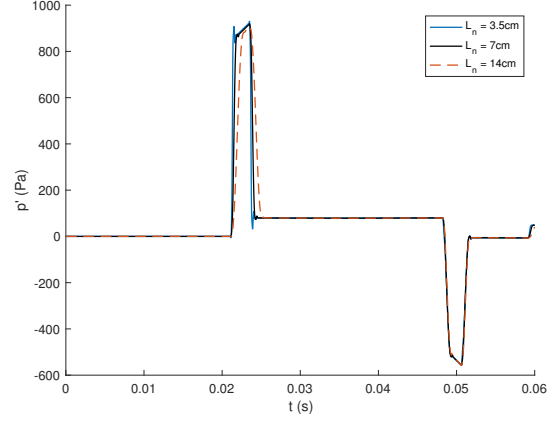


Figure 7.3: Pressure history inside the tunnel at $x = 7.227m$ for L_n varying

A parametric curve of the amplitude of the micro pressure-wave (taken to be the positive jump) is given on (7.4). $L_{ref} = 0.07m$ is the nose length given for the experiment. We can see that, as the length of the nose increases, the amplitude of the pressure-wave decreases. When the nose length is around 15% of the train length, increasing it does no longer have an impact on the micro-pressure wave amplitude. This pattern could not be reproduced by a simple regression model.

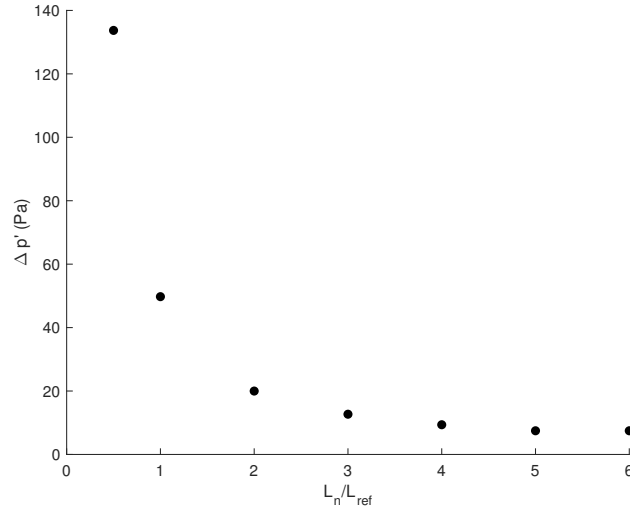


Figure 7.4: Variation of the amplitude of the micro-pressure wave with L_n

We can conclude from this parametric study that increasing to a certain extent the length of the nose of the train, allowing for a smoother entry of the train in the tunnel, reduces the amplitude of the micro-pressure wave. This is backed by figure (7.2) on which we can see that the longer the train nose, the smoother the wave front led by the train. Increasing the nose length of the train can thus help to reduce the noise created at the exit portal.

7.2 Influence of the blockage ratio

We test here several blockage ratio and their impact on the micro-pressure wave.

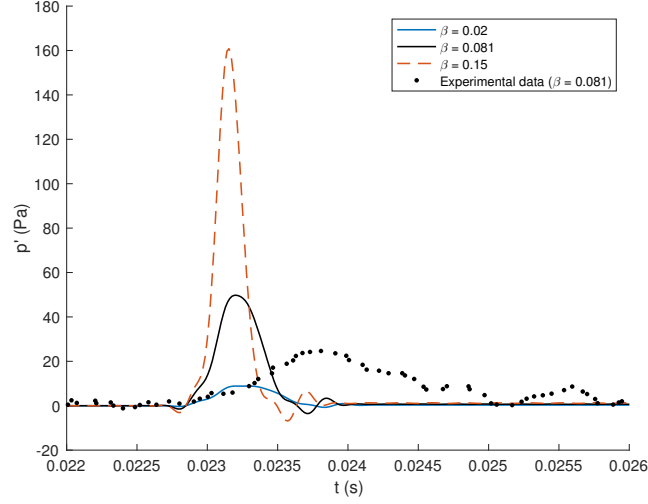


Figure 7.5: Influence of β on the micro-pressure wave shape

The blockage ratio has a dramatic impact on the micro-pressure wave amplitude, while not affecting its time-span, as the nose length parameter can. The larger the blockage ratio, the more compressed will be the tunnel air between the train and the tunnel as figures (7.6) and (7.7) show.

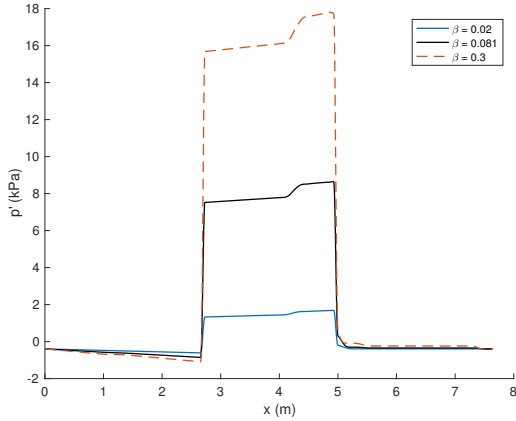


Figure 7.6: Spatial evolution of p inside the tunnel for β varying, at $t = 0.06s$

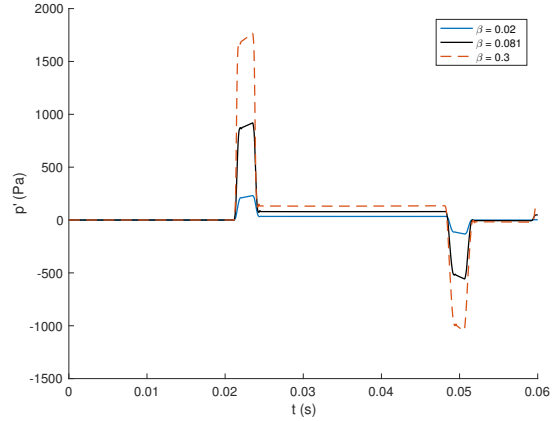


Figure 7.7: Pressure history inside the tunnel at $x = 7.227m$ for β varying

A parametric study of the impact of β on the micro-pressure wave (7.8) can show that the amplitude of the pressure wave increases nearly quadratically with the blockage ratio. We have $\Delta p \propto \beta^2$ with a coefficient of determination obtained is $R^2 = 0.998$. This has also been found in another paper [1].

Reducing the blockage ratio is important to reduce the pressure wave. But since the cross-area of the train is fixed by its functionality (transporting passengers), increasing

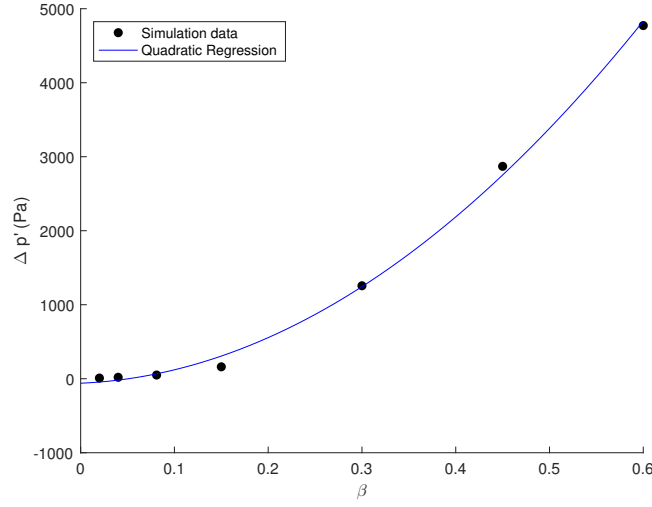


Figure 7.8: Variation of the amplitude of the micro-pressure wave with β

the blockage-ratio means making a bigger tunnel, which is very expensive.

7.3 Influence of the train speed

We test here several train speeds and their impact on the micro-pressure wave. The spatial pressure evolution with V_{Tr} is not shown as the differences between the position of the train inside the tunnel are too important and make the graph unreadable.

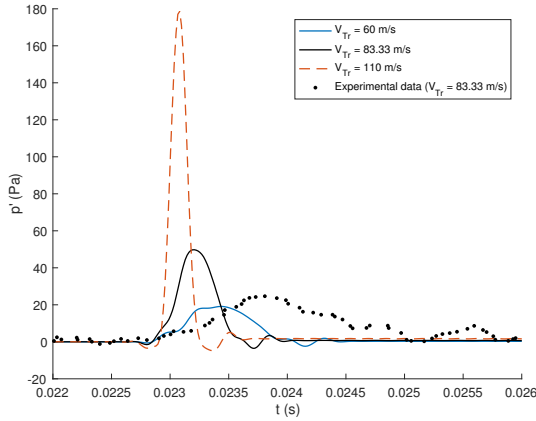


Figure 7.9: Influence of the v_{Tr} on the micro-pressure wave shape

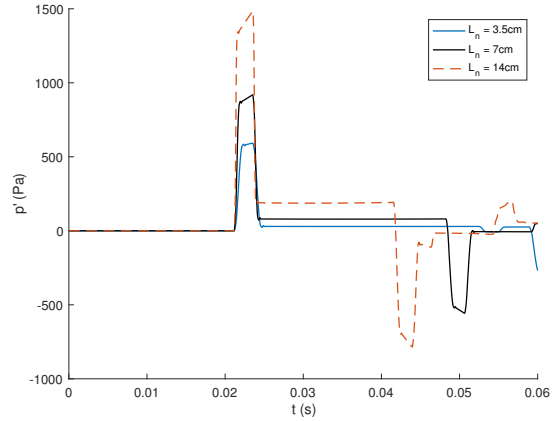


Figure 7.10: Pressure history inside the tunnel at $x = 7.227m$ for V_{Tr} varying

Increasing the speed of the train increases the amplitude of the micro-pressure wave, and also shorten its time-span. The reason is similar to the shortening of the train nose, as increasing the speed will make the train impact into the tunnel static air more abrupt while entering the tunnel, and thus create a stronger compression wave, leading to a bigger micro-pressure wave at the exit portal.

A parametric study can show that $\Delta p \propto V_{Tr}^3$. The determination coefficient obtained is $R^2 = 1$. This has also been observed in the following paper [1].

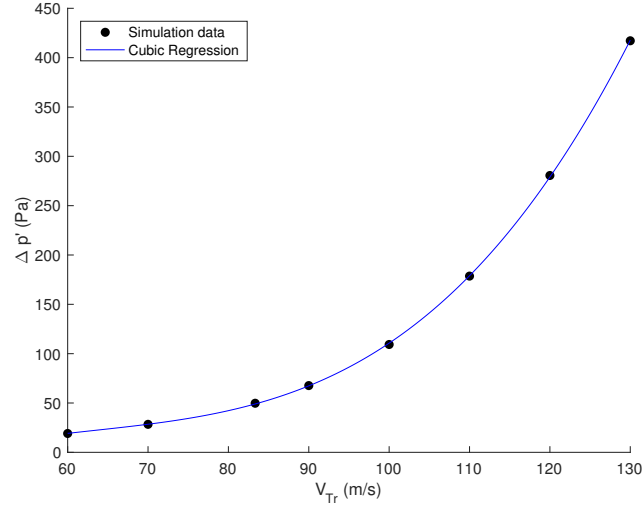


Figure 7.11: Variation of the amplitude of the micro-pressure wave with v_{Tr}

Reducing the train speed before its tunnel entry, which is not too constraining, can thus help reducing the noise created by the train entry into the tunnel.

8 Conclusion

We assessed through this work the ability for the Kirchhoff and Ffowcs-Williams Hawkins equations to reproduce the micro-pressure wave at the exit of a tunnel. We have seen that the two equations are similar, and that both models are sensitive to high frequencies. Reducing the numerically induced oscillations is thus important to get a shape of micro-pressure wave closer to reality. This can be achieved by increasing the number of cells in the mesh and avoid discontinuities on the nose shape of the train, as it creates oscillations. Using the discontinuous Galerkin simulation program we managed, after eliminating the useful but too inaccurate approximation of the integral of both models to a multiplication, to reproduce to a certain extent the experimental data of the NLR. We used the same parameters as in the experiment, at the exception of the nose shape, and got a simulated micro-pressure wave with the same shape, starting at the same time, and with the same amplitude. Though, the presence of a time shift has not been clearly understood. This could come from the different nose shape used in the experiment. Comparing our model with other data sets could prove useful in confirming what has been observed here, and see if there is also a time shift. We were able to reproduce results observed in [1] on the impact of parameters such as the blockage ratio or the train speed on the amplitude of the micro-pressure wave. This parametric study tells us that in order to reduce the tunnel boom noise, increasing the nose length, reducing the train speed or decreasing the blockage ratio are potential solutions.

8 Bibliography

- [1] A. Baron, P. Molteni, and L. Vigevano, “High-speed trains: Prediction of micro-pressure wave radiation from tunnel portals,” *Journal of Sound Vibration*, vol. 296, pp. 59–72, sep 2006.
- [2] C. Biotto, A. Proverbio, O. Ajewole, N. P. Waterson, and J. Peiró, “On the treatment of transient area variation in 1d discontinuous galerkin simulations of train-induced pressure waves in tunnels,” *International Journal for Numerical Methods in Fluids*, vol. 71, no. 2, pp. 151–174, 2013.
- [3] T. Yoon, S. Lee, J. Hwang, and D. Lee, “Prediction and validation on the sonic boom by a high-speed train entering a tunnel,” *Journal of Sound and Vibration*, vol. 247, no. 2, pp. 195 – 211, 2001.
- [4] S. Lee, J. Kim, Y. Yu, and M. Isom, “Prediction of rotor high-speed impulsive noise with a combined cfd-kirchhoff method,” *Journal of sound and vibration*, vol. 207, no. 4, pp. 453–464, 1997.
- [5] J. Prieur and G. Rahier, “Comparison of fflowcs williams-hawkings and kirchhoff rotor noise calculations,” *Office National d’Études et de Recherches Aerospatiales ONERA-PUBLICATIONS-TP*, 1998.
- [6] E. Roux, “Modelling of tunnel sonic boom,” 2014.